applied optics

Calibration and comparison of detection efficiency for free-space single-photon avalanche diodes at 850 nm

Jeongwan Jin,[1,*] Thomas Gerrits,[2] and Angela Gamouras[1]

[1] Metrology Research Centre, National Research Council Canada, Ottawa, Ontario K1A 0R6, Canada
[2] National Institute of Standards and Technology, Gaithersburg, Maryland 20899, USA
*Corresponding author: jeongwan.jin@nrc-cnrc.gc.ca

Received 13 April 2022; revised 23 May 2022; accepted 24 May 2022; posted 24 May 2022; published 8 June 2022

A detection efficiency measurement system for free-space single-photon detectors has been established at the National Research Council (NRC) Canada. This measurement apparatus incorporates an 850 nm fiber laser source and utilizes a double-attenuation and substitution calibration technique. Detection efficiency calibrations of silicon single-photon avalanche photodiodes (SPADs) at incident photon rates in the range of 1.0×10^5 photon counts per second (Cts/s) (36 fW) to 2.1×10^6 Cts/s (734 fW) are SI-traceable through the substitution configuration with a silicon transfer standard detector, calibrated directly using the NRC absolute cryogenic radiometer. The measurement approach taken by the NRC was compared with the SPAD calibration technique implemented at the National Institute of Standards and Technology (NIST) in the United States. The count-rate-dependent detection efficiency of a silicon SPAD was measured at NIST and compared with results from the same SPAD measured at NRC within the range of incident photon rates from 1×10^5 Cts/s to 5×10^5 Cts/s. Comparison of the calibration results shows agreement between the two laboratories within the combined measurement uncertainties.

https://doi.org/10.1364/AO.461154

1. INTRODUCTION

The advent of single-photon detection capabilities has enabled the observation of nonclassical correlation between particles [1] and has led to significant advances in quantum cryptography and measurement science [2,3]. As these quantum technologies rapidly evolve into practical implementations, it has become important to characterize such detection devices in a comprehensive manner to ensure their utility and functionality in different measurement configurations. For these reasons, several national metrology institutes (NMIs) worldwide have recently established detection efficiency calibration systems for free-space single-photon detectors (SPDs) [4,5] as well as for fiber-coupled SPDs [6,7]. Moreover, the European Telecommunication Standards Institute has initiated the standardization of SPD characterization methodologies in the application of quantum encryption [8].

One type of SPD characterization methodology employs the quantum correlation of a photon pair where the detection of one photon heralds the presence of the second photon [9]. The advantage of this method is that it enables detection efficiency calibration without referencing existing measurement standards, i.e., it enables absolute calibration. Despite this inherent benefit, this measurement approach requires two SPDs, one to detect each photon, yielding an efficiency value of the complete detection channel, which includes the transmission of photons through optical components and the efficiency of the SPD itself [9]. A second type of SPD characterization methodology relies on a comparison approach where detection performance is compared with national standard radiometers, traceable to the international system of units (SI). In this case, the optical paths in the apparatus used for measurements of the SPD and of the standard radiometer are typically equivalent, allowing for effects from these experimental variables to be cancelled out. This detector substitution method, including the technique of quantum cloning [10] and of optical attenuation [4], allows for the measured SPD detection efficiencies to be traceable to the SI. The correlation and substitution measurement schemes have already been rigorously compared using a hybrid calibration apparatus, which validated the consistency of the two calibration methods with almost equivalent absolute uncertainties [11]. This verification of these two SPD calibration techniques indicates that either one can be equivalently utilized; however, a large number of NMIs have implemented SPD calibration techniques based on detector substitution due to the relative ease of implementation and flexibility in calibration parameters, including photon wavelength and count rate [4–6,12,13].

In this paper, we report the establishment of a detection efficiency calibration system for free-space SPDs based on the optical attenuation method described in [4]. The measurements are SI-traceable to the NRC's optical power scale through a substitution configuration with a silicon transfer standard detector (TSD), calibrated by the NRC absolute cryogenic radiometer [14]. The calibration of a free-space silicon single-photon avalanche photodiode (SPAD) with independent traceability routes has already been compared between two European countries, Germany and the Czech Republic [15], where the same experiment apparatus was utilized for detection efficiency measurements to compare a double-attenuator measurement technique with the implementation of a low optical flux standard. Here, we compare independent free-space SPD detection efficiency calibration systems between Canada (NRC) and the United States at the National Institute of Standards and Technology (NIST). The calibration system at NIST utilizes a primarily fiber-coupled design with variable fiber attenuators, as described in [6]. Comparison measurements of a silicon SPAD at NRC and NIST reveal the robustness of the substitution and attenuation calibration technique over dissimilar platforms with independent SI traceability, a crucial step toward SPD calibration standards in North America.

2. SI-TRACEABLE SINGLE-PHOTON DETECTION EFFICIENCY MEASUREMENTS

The detector substitution technique enables an SPD to be directly compared with a TSD with traceability to the SI, in this case through NRC's optical radiant power scale (Fig. 1). The TSD is directly calibrated by the NRC absolute cryogenic radiometer in a free-space optical configuration in the microwatt power range. The spectral response of the TSD is determined using a tungsten-halogen lamp and double-subtractive monochromator system [14]. The TSD used in this work is a single-element Si detector mounted in an NRC-designed housing with a vacuum compatible quartz window [16]. This design allows for the TSD to be mounted on a customized vacuum flange compatible with the cryogenic radiometer system as well as for use in calibration measurements in air with other room temperature detectors. The uncertainty budget for the TSD is shown in Table 1.

For SPD detection efficiency calibration, the detector substitution method is combined with a double attenuation technique [4]. In this approach, the detection efficiency of the SPD under test is calibrated by measuring the input optical signal with

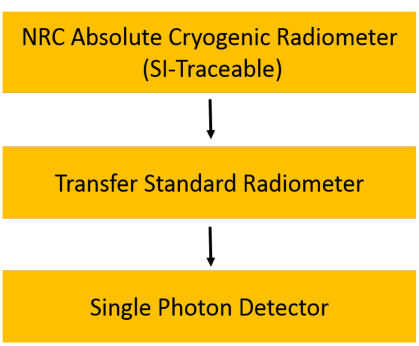

Fig. 1. NRC traceability chain. A transfer standard radiometer, with SI-traceable calibration by means of the NRC primary cryogenic radiometer, is used to calibrate SPD detection efficiencies.

Table 1. Uncertainty Budget for TSD Spectral Responsivity Calibration at 850 nm with 4.5 nm Spectral Bandwith

Source	Magnitude (%)
Cryogenic radiometer effects	0.011
Measurement repeatability	0.131
TSD temperature variation (±1°C)	0.001
TSD photocurrent measurement	0.004
Wavelength calibration (±0.05 nm)	0.003
Spectral bandwidth effects	0.000
Combined uncertainty ($k = 1$)	0.132

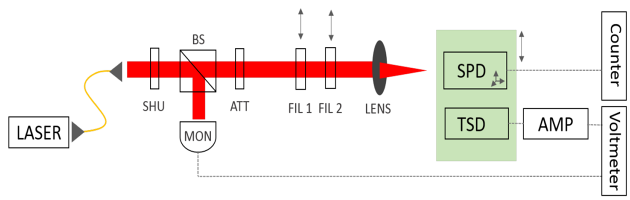

Fig. 2. Diagram of NRC free-space SPD detection efficiency measurement setup. Various levels of incident photon flux are prepared by a variable optical attenuator (ATT) at the input of the calibration apparatus. The power stability of the laser is measured using a beam splitter (BS) and monitor photodiode (MON). Two neutral density filters (FILs) reduce the input flux to the fW level. SHU, shutter; BS, beam splitter; AMP, transimpedance amplifier.

the SPD and with the SI-traceable TSD. Two neutral density filters are employed in order to reduce the input optical power down to a level measurable by the SPD, on the order of 100 fW. One advantage of this method is that the separate transmission calibration of the filters is not required as the TSD measures the signal from the incident photons with and without the filters in the optical path, i.e., *in situ* filter calibration.

The calibration setup is depicted in Fig. 2. The light source is a fiber-coupled continuous wave (CW) laser centered at 850.6 nm (FWHM 126 pm). A beam splitter and silicon photodiode are used to monitor the stability of the laser source throughout the duration of the measurements. The signals from the monitor detector are used as normalization factors for each data point to compensate for any laser power and beam splitter instability in the detection efficiency calibration. Different input laser powers are prepared by a variable optical attenuator, made of various neutral density filters mounted on two independent filter wheels, in the optical path. The prepared input optical signal is focused by an achromatic lens onto the active detection window of the SPD under test or of the TSD. These two detectors, mounted next to each other on the same automated linear translation stage, are carefully aligned to the center of the laser propagation axis for substitution calibration measurements. To calibrate the detection efficiency of the SPD, the number of photons in the input laser light is first measured by the SPD with two neutral density filters (optical densities 3.0 and 4.0) in the optical path in front of the detector. Next, the optical power of the same input laser signal is measured by the TSD with no filters and, subsequently, with each individual filter in the optical path. This measurement sequence only requires a single movement of the translation stage, minimizing uncertainties due to the alignment of the SPAD. Faulty detection events and detector dark counts, mainly due to detector noise and background stray light, are evaluated by blocking the input optical signal with a shutter prior to all measurements and are subtracted from the collected data. These measurements, along with the calibrated TSD responsivity and other parameters, are used to calculate the SPD detection efficiency.

The detection efficiency η of the SPAD, the SPD under test, is determined using Eq. (1), where $E_{\text{single photon}}$ is the energy of a single photon, N_{det} is the number of detected photons, E_{in} is the total energy of the input light field at the front face of the SPAD, and E_0 is the total initial light energy in the absence of the filters with transmission values $T_{i(i=1,2)}$. h, c, and λ denote the Planck constant, the speed of light, and the wavelength of the laser, respectively:

$$\eta_{\text{det}} = \frac{E_{\text{single photon}} \times N_{\text{det}}}{E_{\text{in}}} = \frac{(hc/\lambda) \times N_{\text{det}}}{E_0 \times \prod_{n=1}^{2} T_i}. \quad (1)$$

The energy of the incident laser beam is determined by measuring the voltage signal from the transimpeadance amplifier connected to the TSD. This voltage is then normalized with respect to the signal measured by the monitor photodiode ($Q_0 = V_0/V_{0,Mon}$). Similarly, the input beam with each individual filter in the optical path (Q_1 and Q_2) is then measured by the TSD. Together, with the normalized photon number $Q_3 = N_{SPAD}/V_{SPAD,Mon}$, Eq. (1) can be rewritten as

$$\eta_{\text{det}} = (hc/\lambda) \times s \times \left(\frac{A_1 A_2}{A_0}\right) \times \left(\frac{Q_0}{Q_1 Q_2}\right) \times Q_3, \quad (2)$$

where s is the spectral response of the TSD. Here, s was calibrated in the μW optical power range, but this calibration is valid for the various input power levels used in our measurements due to linear detector characteristics with negligible uncertainty contributions [17]. $A_{i(i=0,1,2)}$ are amplification factors of the TSD where the subscripts 0, 1, and 2 represent the presence of no, Filter 1, and Filter 2 in the optical path, respectively.

The probability that the SPAD undergoes a detection event, or click, is given by $P_{\text{det}(N\geq 1)} = 1 - P_0$, where P_0 is the probability of not detecting any photons. For a Poissonian light field with a photon-number distribution of $P_N = \mu^N e^{-\mu}/N!$, the probability can be rewritten as

$$P_{\text{det}(N\geq 1)} = 1 - \exp(-\eta_{\text{ideal}}\mu) = \eta_{\text{det}}\mu \quad (3)$$

for the given mean photon number $\mu \leq 1$. Here, η_{ideal} denotes the ideal value of the SPD detection efficiency without any detection artifacts, such as the detection reset time or afterpulsing. Ideally, only one output signal is generated by the detection of a single photon, and no photon enters the detector during inactive periods. The measured detection efficiency is then represented by [4,18]

$$\eta_{\text{det}} = \frac{1 - e^{(-\eta_{\text{ideal}}\mu)}}{\mu}. \quad (4)$$

For our implementation with a CW laser, the upper bound of the mean photon number is given by $\mu = \mathrm{N}/\mathrm{N}_{\mathrm{ON}}^{\max} \leq (\mathrm{N}_{\text{det}}/\eta_{\text{det}})\Delta t_{\text{OFF}}$, where N is the number of photons present, N_{det} is the number of photons detected by the SPAD, and $\mathrm{N}_{\mathrm{ON}}^{\max}$ is the maximum number of detection events with SPAD recovery time Δt_{OFF} (the sum of detector dead time and reset time). As defined in [18], dead time is the time interval in which the detector is not capable of generating an output signal in response to incoming single photons, and reset time is the amount of time required for the detector to return to a baseline value after a detection event. The detection efficiency decreases with larger count rates, as an increasing number of photons is not detected during the detector recovery time. Additionally, as a click/no-click detector, the SPAD cannot resolve the number of photons present, and multidetection events are only registered as a single detector click.

3. MEASUREMENT UNCERTAINTIES AND RESULTS

Prior to performing detection efficiency measurements, the spatial uniformity of the SPAD is scanned using an automated 3D translation stage and the incident laser light. The active detection area of a free-space SPAD is typically small, and spatial uniformity measurements are used to ensure the accurate alignment of the focused laser beam within the active area of the detector. To capture all of the incident light within the active area of the SPAD, a 75 mm focal length achromatic lens focuses the beam down to a 17 μm diameter spot. Once the spatial uniformity measurement is completed, the 3D translation stage positions the center of the SPAD detection window in the optimal position and completes all SPAD-relevant measurements. The automated linear translation stage is then used to position the center of the TSD to the laser beam for the remaining measurements. Since the SPAD active area is approximately 160 μm, a slight misalignment of the beam would introduce a significant error in the measurement. The spatial uniformity of the SPAD used in the NRC and NIST comparison measurements is shown in Fig. 3.

The uncertainty budget of the SPAD detection efficiency measured at a count rate of 1×10^5 counts per second (Cts/s) in the NRC facility is summarized in Table 2. The same amplification $A(A1 = A2 = A3)$ was used for the determination of all three Q values measured with the TSD. The combined uncertainty was evaluated by standard error propagation

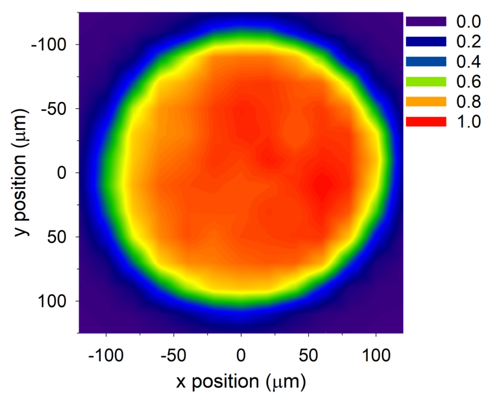

Fig. 3. Spatial uniformity of the SPAD under test measured at NRC with a normalized count rate.

Table 2. NRC Uncertainty Budget of Measured Detection Efficiency at $N_{SPAD} = 102895$ Counts per Second

Measurand	Unit	Measured Value	Uncertainty	Type	Uncertainty (%)
Speed of light (c)	$m \cdot s^{-1}$	2.99792458×10^{8}			
Planck constant (h)	$J \cdot s$	$6.62607015 \times 10^{-34}$			
Wavelength (λ)	m	850.63×10^{-9}	6.00×10^{-11}	B	0.01
TSD spectral responsivity (s)	$A \cdot W^{-1}$	4.53×10^{-1}	5.98×10^{-4}	A	0.13
Amplification (A_0, A_1, A_2)	$V \cdot A^{-1}$	1.00×10^{9}	5.00×10^{6}	B	0.50
Ratio $V_0/V_{0,Mon}$ (Q_0)	1	1.14×10^{1}	8.38×10^{-3}	A	0.07
Ratio $V_1/V_{1,Mon}$ (Q_1)	1	2.25×10^{-1}	7.53×10^{-4}	A	0.34
Ratio $V_2/V_{2,Mon}$ (Q_2)	1	2.64×10^{-2}	7.31×10^{-4}	A	2.76
Ratio $N_{SPAD}/V_{SPAD,Mon}$ (Q_3)	$V^{-1} \cdot s^{-1}$	2.25×10^{6}	8.05×10^{3}	A	0.32
Detection efficiency (η_{det})	1	5.09×10^{-1}	1.45×10^{-2}	A	
Combined uncertainty ($k = 1$), $u(\eta_{det}^{NRC})$					2.85

$$\frac{\Delta \eta_{det}}{\eta_{det}} = \sqrt{\left(\frac{\Delta\lambda}{\lambda}\right)^2 + \left(\frac{\Delta s}{s}\right)^2 + \left(\frac{\Delta A}{A}\right)^2 + \sum_{i=0}^{3}\left(\frac{\Delta Q_i}{Q_i}\right)^2}. \tag{5}$$

$\Delta\lambda$ and ΔA were calibrated by the utilized optical spectrum analyzer and transimpedance amplifier manufacturers Thorlabs and Gentec International, respectively. The largest contributions to the measurement uncertainty are due to the transimpedance amplifiers used in conjunction with the TSD and the monitor detector. At the fW power level, the signal-to-noise ratios in the voltage measurements from these detectors and amplifiers are the limiting factors in the present calibration setup. The combined uncertainty listed in Table 2 is representative for lower photon flux measurements with the NRC apparatus; however, in the 1×10^6 Cts/s range, the combined uncertainty decreases to 0.6%.

As a method of validation of the free-space SPAD calibration setup at NRC, a Si-SPAD (PerkinElmer SPCM-AQRH-13 serial no. 21017) was measured at both NRC and at NIST, with independent SI-traceability through each NMI. The calibration apparatus at NIST is also based on an attenuation and substitution technique and utilizes a 851 nm laser source. The main distinction between the two calibration setups is the use of free-space neutral density filters at NRC and of variable optical fiber attenuators at NIST. The NIST calibration apparatus and complete uncertainty budget are described in detail in [6]. The detection efficiency of the SPAD under test was measured within the range of incident photon count rates of 1.0×10^5 Cts/s to 2.1×10^6 Cts/s, corresponding to a range of mean photon numbers from $\mu = 0.025$ to $\mu = 0.52$, at NRC and within the range of 3.0×10^4 Cts/s to 5.0×10^5 Cts/s at NIST. The data from each laboratory were fit using a commercially available data analysis software package. Equation (4), which includes the relation $\mu = (N_{det}/\eta_{det})\Delta t_{OFF}$, is plotted along with the calculated mean photon numbers in Fig. 4. Despite the error bars caused by amplifier noise in the NRC data at low input photon rates, the NRC and NIST fitting curves are in good agreement. By fitting the NRC and NIST data using Eq. (4), we find the detector recovery time of $\Delta t_{OFF}^{NRC} = 123 \pm 22$ ns and $\Delta t_{OFF}^{NIST} = 130 \pm 10$ ns as well as the ideal detection efficiency of $\eta_{ideal}^{NRC} = 0.535 \pm 0.004$ and $\eta_{ideal}^{NIST} = 0.534 \pm 0.0004$.

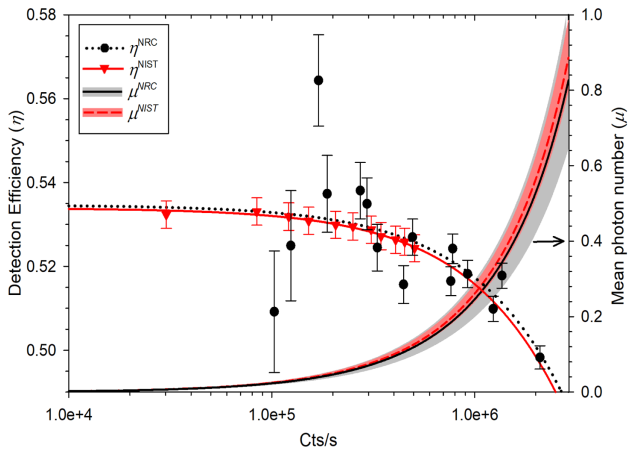

Fig. 4. SPAD detection efficiencies measured at NRC and NIST. The uncertainty in the mean photon numbers is represented by the shaded regions on the graph.

The agreement between the NRC and NIST measurements was evaluated using an unmediated consistency test as well as by calculating a comparison reference value (CRV). The detection efficiency values considered for the evaluation of laboratory equivalence were selected based on the proximity of the measured photon counts rates. The difference between the NRC and NIST SPAD signal values listed in Table 3 are all <20%. The variation between the measurement results, without any statistical estimators, was calculated using Eq. (6) and is shown in Fig. 5 with the combined laboratory uncertainties:

$$\Delta = \frac{\eta_{det}^{NIST} - \eta_{det}^{NRC}}{\left(\eta_{det}^{NIST} + \eta_{det}^{NRC}\right)/2}. \tag{6}$$

The CRV, η_{ref}, was calculated using the weighted mean of the measurements:

$$\eta_{ref} = \frac{\eta_{det}^{NIST} u^{-2}\left(\eta_{det}^{NIST}\right) + \eta_{det}^{NRC} u^{-2}\left(\eta_{det}^{NRC}\right)}{u^{-2}\left(\eta_{det}^{NIST}\right) + u^{-2}\left(\eta_{det}^{NRC}\right)}, \tag{7}$$

where $u(\eta_{det}^{NIST})$ and $u(\eta_{det}^{NRC})$ are the standard uncertainties of η_{det}^{NIST} and η_{det}^{NRC}, respectively. The deviation of the measurements from each laboratory from the CRV:

$$d_{Lab} = \eta_{det}^{Lab} - \eta_{ref}, \tag{8}$$

Table 3. NRC and NIST Comparison Results of SPAD Detection Efficiencies

NRC			NIST			Normalized Error		
SPAD Signal (Cts/s)	Detection Efficiency	Standard Uncertainty	SPAD Signal (Cts/s)	Detection Efficiency	Standard Uncertainty	Unmediated Err	Relative to CRV Err_{NRC}	Err_{NIST}
494352	0.527	0.004	490879	0.524	0.003	0.24	0.12	0.08
446310	0.516	0.005	439989	0.526	0.003	0.92	0.47	0.27
331550	0.524	0.006	326821	0.529	0.003	0.36	0.20	0.08
294975	0.535	0.006	292509	0.529	0.003	0.41	0.24	0.08
273072	0.538	0.007	270240	0.529	0.003	0.59	0.36	0.10
187470	0.537	0.009	179168	0.530	0.003	0.37	0.24	0.04
169977	0.564	0.011	151944	0.531	0.003	1.47	0.97	0.12
124033	0.525	0.013	121060	0.532	0.003	0.26	0.17	0.01
102895	0.509	0.015	84364	0.533	0.003	0.80	0.55	0.04

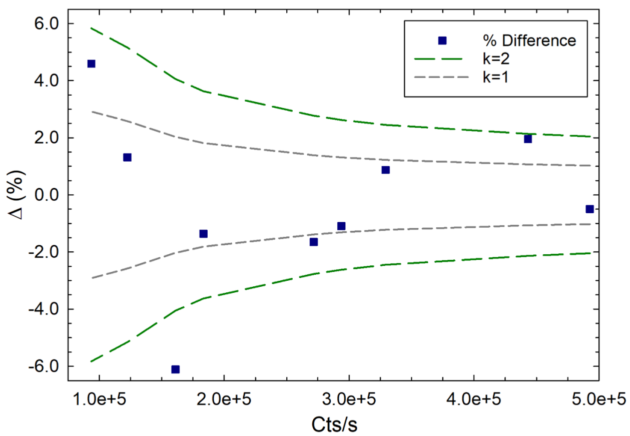

Fig. 5. Unmediated comparison of NRC and NIST SPAD detection efficiency measurements and combined laboratory uncertainties with expansion factors $k = 1$ and $k = 2$.

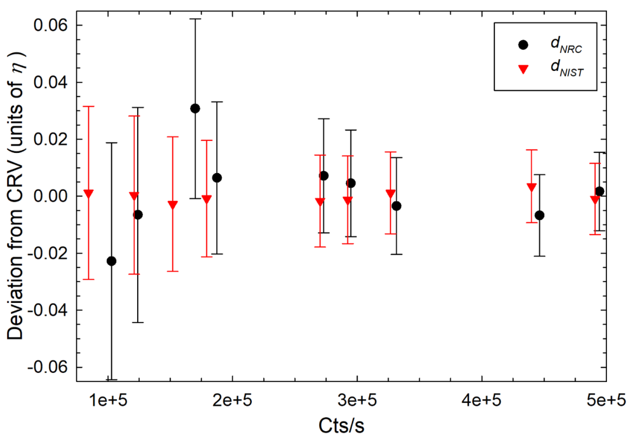

Fig. 6. Deviation of NRC and NIST SPAD detection efficiency measurements from the CRV. Error bars indicate uncertainties with expansion factor $k = 2$ [Eq. (9)].

and the associated uncertainties

$$U(d_{\text{Lab}}) = k\left(\sqrt{u^2(\eta_{\text{det}}^{\text{Lab}}) + u^2(\eta_{\text{ref}})}\right), \tag{9}$$

are shown in Fig. 6.

The normalized error (Err), routinely used in interlaboratory proficiency testing where Err < 1 indicates measurement consistency, was implemented to assess the degree of equivalence and the quality of the compared detection efficiency values [19]. Considering unmediated comparison analysis (Err) is given by

$$\text{Err} = \frac{|\eta_{\text{det}}^{\text{NIST}} - \eta_{\text{det}}^{\text{NRC}}|}{\sqrt{U^2\left(\eta_{\text{det}}^{\text{NIST}}\right) + U^2\left(\eta_{\text{det}}^{\text{NRC}}\right)}}. \tag{10}$$

Using the CRV, Err becomes

$$\text{Err}_{\text{Lab}} = \frac{|\eta_{\text{det}}^{\text{Lab}} - \eta_{\text{ref}}|}{\sqrt{U^2(\eta_{\text{det}}^{\text{Lab}}) + U^2(\eta_{\text{ref}})}}. \tag{11}$$

The calculated Err values for the data shown in Table 3 indicate that the NRC and NIST SPAD comparison results are metrologically equivalent within the combined laboratory uncertainties, with the exception of one data point at the NRC SPAD signal of 169977 Cts/s. This anomaly is most likely due to poor signal to noise, mainly caused by electronic noise from the transimpedance amplifier used in conjunction with the TSD during measurements at NRC.

4. CONCLUSION

We have demonstrated a free-space SPD calibration apparatus with SI-traceability through the optical power scale at NRC Canada. This automated measurement system implements a detector substitution and double-attenuation calibration technique and has the capability to determine the spatial uniformity of the active area of the SPD under test. Results from the NRC calibration setup were compared with the SPD calibration system established at NIST by measuring the detection efficiency of the same Si-SPAD with a common range of input photon rates from 1×10^5 Cts/s to 5×10^5 Cts/s. The measured average detection efficiencies and normalized error values indicate agreement between the laboratories within the measurement uncertainties and with independent SI-traceablity. Measurement uncertainties for SPAD detection efficiency calibrations at NRC can be improved by utilizing alternative low-noise and high-gain TSD and monitor detector signal amplifiers and potentially an alternate attenuation technique, such as optical fiber-based attenuators, to achieve lower incident photon count rates.

Acknowledgment. The commercial equipment identified in this paper is for informative purposes only. Such identification does not imply a recommendation or endorsement by NRC or NIST, nor does it imply that the equipment is necessarily the best available for the purpose.

Disclosures. The authors declare no conflicts of interest.

Data availability. Data underlying the results presented in this paper are not publicly available at this time but may be obtained from the authors upon reasonable request.

REFERENCES

1. S. J. Freedman and J. F. Clauser, "Experimental test of local hidden-variable theories," Phys. Rev. Lett. **28**, 938–941 (1972).
2. N. Gisin, G. Ribordy, W. Tittel, and H. Zbinden, "Quantum cryptography," Rev. Mod. Phys. **74**, 145–195 (2002).
3. J. P. Dowling, "Quantum optical metrology–the lowdown on high-NOON states," Contemp. Phys. **49**, 125–143 (2008).
4. M. López, H. Hofer, and S. Kück, "Detection efficiency calibration of single-photon silicon avalanche photodiodes traceable using double attenuator," J. Mod. Opt. **62**, S21–S33 (2015).
5. I.-H. Bae, S. Park, K.-S. Hong, H. S. Park, H. J. Lee, H. S. Moon, J. S. Borbely, and D.-H. Lee, "Calibration of free-space and fiber-coupled single-photon detectors," Metrologia **56**, 035003 (2019).
6. T. Gerrits, A. Migdall, J. C. Bienfang, J. Lehman, S. W. Nam, J. Splett, I. Vayshenker, and J. Wang, "Calibration of free-space and fiber-coupled single-photon detectors," Metrologia **57**, 015002 (2019).
7. H. J. Lee, S. Park, H. S. Park, K. S. Hong, D.-H. Lee, H. Kim, M. Cha, and H. S. Moon, "Wavelength-scanning calibration of detection efficiency of single photon detectors by direct comparison with a photodiode," Metrologia **53**, 908–917 (2016).
8. "QKD component characterization: characterizing optical components for QKD system," ETSI GS QKD 011 (ETSI2016).
9. S. V. Polyakova and A. L. Migdall, "Quantum radiometry," J. Mod. Opt. **56**, 1045–1052 (2009).
10. B. Sanguinetti, E. Pomarico, P. Sekatski, H. Zbinden, and N. Gisin, "Quantum cloning for absolute radiometry," Phys. Rev. Lett. **105**, 080503 (2010).
11. S. V. Polyakov and A. L. Migdall, "High accuracy verification of a correlated-photon-based method for determining photon-counting detection efficiency," Opt. Express **15**, 1390–1407 (2007).
12. I. Müller, R. M. Klein, J. Hollandt, G. Ulm, and L. Werner, "Traceable calibration of Si avalanche photodiodes using synchrotron radiation," Metrologia **49**, S152–S155 (2012).
13. I. Müller, R. M. Klein, and L. Werner, "Traceable calibration of a fibre-coupled superconducting nano-wire single photon detector using characterized synchrotron radiation," Metrologia **51**, S329–S335 (2014).
14. A. Gamouras, A. D. W. Todd, É. Côté, and N. L. Rowell, "The development of the advanced cryogenic radiometer facility at NRC," J. Phys. Conf. Ser. **972**, 012014 (2018).
15. G. Porrovecchio, M. Šmid, M. López, H. Hofer, B. Rodiek, and S. Kück, "Comparison at the sub-100 fW optical power level of calibrating a single-photon detector using silicon photodiode and the double attenuator technique," Metrologia **53**, 1115–1122 (2016).
16. L. P. Boivin and K. Gibb, "Monochromator-based cryogenic radiometry at the NRC," Metrologia **32**, 565–570 (1995).
17. L. P. Boivin, "Measurements using two types of transfer radiometer developed for a monochromator-based cryogenic radiometer facility," Metrologia **35**, 363–368 (1998).
18. C. J. Chunnilall, I. P. Degiovanni, S. Kück, I. Müller, and A. G. Sinclair, "Metrology of single-photon sources and detectors: a review," Opt. Eng. **53**, 081910 (2014).
19. A. Steele and R. J. Douglas, "Extending E_n for measurement science," Metrologia **43**, S235–S243 (2006).